AUTHOR QUERY FORM

ELSEVIER	**Book: Borenstein1610687** **Chapter: CH005**	**Please e-mail your responses and any corrections to:** **E-mail: p.wilkinson@elsevier.com**

Dear Author,

Any queries or remarks that have arisen during the processing of your manuscript are listed below and are highlighted by flags in the proof. (AU indicates author queries; ED indicates editor queries; and TS/TY indicates typesetter queries.) Please check your proof carefully and answer all AU queries. Mark all corrections and query answers at the appropriate place in the proof (e.g., by using on-screen annotation in the PDF file http://www.elsevier.com/framework_authors/tutorials/ePDF_voice_skin.swf) or compile them in a separate list, and tick off below to indicate that you have answered the query.
Please return your input as instructed by the project manager.

Uncited references: References that occur in the reference list but are not cited in the text. Please position each reference in the text or delete it from the reference list.	
Missing references: References listed below were noted in the text but are missing from the reference list. Please make the reference list complete or remove the references from the text.	

Location in Article	Query / remark	
AU:1, Page 120	Please rephrase the sentence "These let us..." for clarity.	
AU:2, Page 124	Please expand ESCA, if needed.	
AU:3, Page 127	We have retained the usage of hyphens for CD-time and CD-ratio. Please confirm.	
AU:4, Page 131	Please provide place of publication.	
AU:5, Page 134	Please provide the place of publication.	
AU:6, Page 134	Please provide place of publication.	
AU:7, Page 129	Please check the sentence "Optical sequential..." for clarity.	
AU:8, Page 104	Please check and confirm the verso page running head cut shortening.	
AU:9, Page 109	Please check and confirm the caption continued style.	

CHAPTER

5

c0005

Mechanobiological Approaches for the Control of Cell Motility

s0010 ## 5.1 Introduction

p0025 Cell movement is a multistep process that results from concerted biological queues such as environmental factors, signal transduction, and cytoskeletal rearrangement. The migratory behavior of an adherent cell is known as a sequential combination of the following processes: the morphological polarization of a cell into a teardrop shape; the extension of the cell membrane; the formation of cell−substrate adhesions at a leading edge; the translocation of the cell body via contractile force; the detachment of cell−substrate adhesions at a trailing edge. Directed cell motility is essential to the development and maintenance of multicellular organisms which require the orchestrated movement of adherent cells to specified sites in particular directions [1]. Any abnormality in cell motility is known to lead to serious pathophysiological consequences such as mental retardation, vascular disease, tumor formation, and metastasis [2]. A better control of cell motility therefore has a major impact on the development of new therapeutic strategies for the pathophysiological consequences. For example, a successful control of cell motility can lead to the development of new medical dressings for fast wound healing. In detail, fibroblasts and epithelial cells move intensively toward open wounds during wound healing process, especially proliferation phase [3,4]. If this chemotactic cell movement is controlled (i.e., expedited with controllability), then the wound healing process will be significantly promoted.

p0030 Due to the biological importance of cell motility in pathophysiological phenomena, many studies have been intensively conducted to understand the migratory behavior of adherent cells. Previous microelectromechanical systems (MEMS)-based approaches have primarily addressed the effect of chemically and topographically patterned substrates on cell−substrate interactions that regulate cell motility [5]: microscale (isotropic and anisotropic) chemical patterns on a variety of substrates were used to characterize cell patterning and growth along the patterns [7] which were closely related to cell motility, and nanoscale (isotropic and anisotropic) chemical patterns were utilized to regulate collective cell functions such as migration, adhesion, proliferation, and differentiation [8,9]; (micro and nano) isotropic

103

topographical patterns (e.g., evenly or randomly distributed pits or protrusions) were fabricated to examine the collective cell functions [10,11], and (micro and nano) anisotropic topographical patterns (e.g., parallel troughs and ridges) were to understand cell alignment along the patterns [12,13]. Although these attempts were successful in characterizing the effect of chemical and topographical patterns on the migratory behavior of adherent cells, their success was far from controlling cell motility (e.g., direction and rate of cell movement).

p0035   Recently, controlling the direction and rate of cell movement has been found to have a prominent association with new therapy developments for diseases such as cardiovascular diseases, asthma, and cancer. To meet the needs of the time, several passive methods using MEMS technology were developed to control the motility of adherent cells. At first, "wound healing" assays were developed to manipulate cell movement. The assays involved deliberately inflicting wounds on a confluent monolayer of adherent cells [14−16]. They induced the cells to spontaneously polarize and migrate toward the wounds. However, these assays showed very limited controllability of cell movement—no control for the movement path of adherent cells. Since Harrison [17] found cell responses to solid structures (i.e., contact guidance), a control for cell motility using a variety of topographical features has been extensively researched. For example, parallel grooves [18−21], spikes [22], three-dimensional post arrays [23], meshes [24], and porosities [25,26] were used to enhance cell movement along the topographical features and to suppress cell movement across them. However, these methods were still far from a full control of cell movement, i.e., moving an adherent cell to a specified site in a particular direction. Active methods using MEMS technology were also carried out to regulate cell movement. Chemotactic assays [27−32] were the mainstream in these approaches. The assays adjusted the concentration distribution of chemoattractants (or chemorepellents) using two microchambers connected to each other through a microvalve. For example, cells and chemoattractants (or chemorepellents) were placed in each of the chambers and the gradient of chemical signals around the cells was manipulated by regulating the microvalve. Although the chemotactic assays somewhat controlled cell movement, they were unable to control cell motility at a single-cell level. Moreover, the assays depended on the use of active microdevices (e.g., microvalves and microregulators) which placed restrictions on the extent of their biomedical applications. As a slightly different approach, various experimental techniques which manipulate cell detachment (or cell adhesion) were developed to control the motility of adherent cells. The techniques can be categorized into photolithography [33,34], e-beam lithography [35], dip-pen lithography [36], nanoimprint lithography [37], microcontact printing [38,39], elastomeric stencil [40], ink-jet printing [41], and optical tweezer [42]. Although these techniques successfully manipulated cell detachment (or cell adhesion), they failed to show a concrete evidence of controlled cell movement. Furthermore, these techniques applied unintended mechanical stimuli (e.g., cell denaturation [42]) to cells and considerably deformed the cells before and during experiment.

p0040   In this chapter, we present two mechanobiological approaches using MEMS technology, each of which respectively manipulates cell motility in passive and active ways. As a passive approach, a biological assay carved with diverging micropatterns, termed "Rome platform," which makes all adherent cells lead to the Rome (target site) is developed. This method has the following specialties in controlling the motility of adherent cells. First of all, this controls the rate and direction of cell movement by imposing one-directional morphological polarity on adherent cells with diverging micropatterns, which is as similar as possible to *in vivo* cell movement. This method therefore makes it possible to manipulate the movement of *undisturbed* adherent cells. Additionally, this controls cell movement in a *passive* way, i.e., by adjusting the dimensions of diverging micropatterns. To control the motility of adherent cells in an active way, one part of an adherent cell is selectively detached from a substrate using a mechanobiological assay, nicknamed "biological breadboard (BBB)." This assay spatiotemporally manipulates cell detachment at a subcellular level using the reductive desorption of a gold−thiol self-assembled monolayer (SAM) at a negative activation potential of −0.9 to −1.65 V. This assay has the following features in manipulating cell movement. This controls the migratory behavior of *living and intact* cells. By employing an arginine−glycine−aspartic (RGD) peptide as a cell adhesion motif, the BBB provides adherent cells with a microenvironment that is as similar as possible to *in vivo* microenvironment. This is because a microenvironment is one of the most dominant factors in determining the motility of adherent cells.

s0015 5.2 Passive control of cell motility

s0020 5.2.1 Rome platform

p0045 A Rome platform consists of parallel and narrow troughs (zone I), diverging troughs (zone II), and parallel and wide troughs (zone III), as shown in Figure 5.1. The dimensions of the diverging micropatterns are chosen to be trough depth (or ridge height) of 3 μm, divergence angle of 0.5−5.0°, and width of trough/ridge of 3−10 μm. As the dimensions are within a range comparable with cell (especially, NIH 3T3 fibroblasts) size, the migratory behavior of the cells is significantly influenced by the diverging micropatterns.

p0050   The diverging micropatterns achieve one-directional cell movement by imposing one-directional morphological polarity on adherent cells. The working principle of the Rome platform, ~~directed cell movement in a passive way~~, can be explained by both cell biology and fluid mechanics. An adherent cell on the diverging micropatterns senses microscopic structural nonuniformities (i.e., diverging troughs and ridges), and starts to change its morphology into a teardrop shape (Figure 5.2A). This change in cell morphology makes the cell move into the diverging direction [1,43]. Even when a cell initially travels in the opposite direction (i.e., converging direction), the diverging micropatterns make the cell
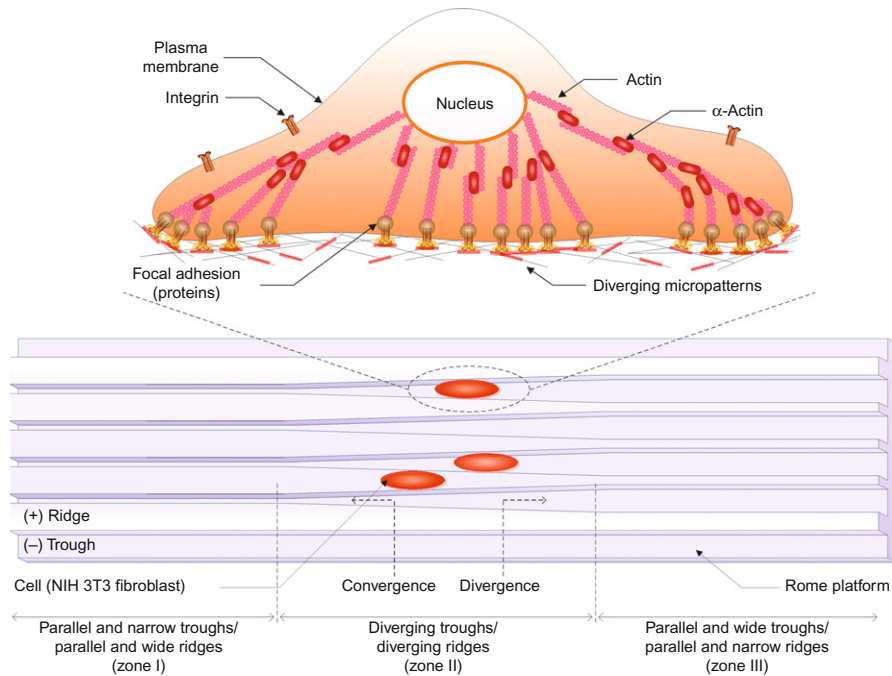
f0010

FIGURE 5.1

A biological assay carved with diverging micropatterns, termed "Rome platform," to control cell movement in a passive way. The Rome platform is composed of parallel and narrow troughs (zone I), diverging troughs (zone II), and parallel and wide troughs (zone III). The zone II has different angles of 0.5°, 1.0°, 2.0°, 4.0°, and 5.0° and two widths of trough/ridge of 3 μm (beginning of divergence) and 10 μm (end of divergence). This assay imposes one-directional morphological polarity on adherent cells using the zone II, thus manipulating the motility of adherent cells.

change its movement direction (Figure 5.2B, C). That is, the microscopic structural nonuniformities of the diverging micropatterns apply one-directional spatial stimuli to the cell through cell−substrate interactions, thus forcing the cell to move in a specified direction.

p0055   From a fluid mechanics viewpoint, cell movement in a diverging micropattern (Figure 5.2A, bottom) is assumed as a viscous flow in a rectangular microchannel with a channel length of l_{ch}, a width of w_{ch}, and a height of h_{ch}. The flow resistance in the microchannel, Ω_{ch}, is expressed as

$$\Omega_{ch} = \frac{12\eta l_{ch}}{h_{ch}{}^3 w_{ch}} \left\{ 1 - \sum_{n=1,3,5,\ldots}^{\infty} \frac{1}{n^5} \frac{192}{\pi^5} \frac{h_{ch}}{w_{ch}} \tan h\left(\frac{n\pi w_{ch}}{2h_{ch}} \right) \right\}^{-1} \tag{5.1}$$
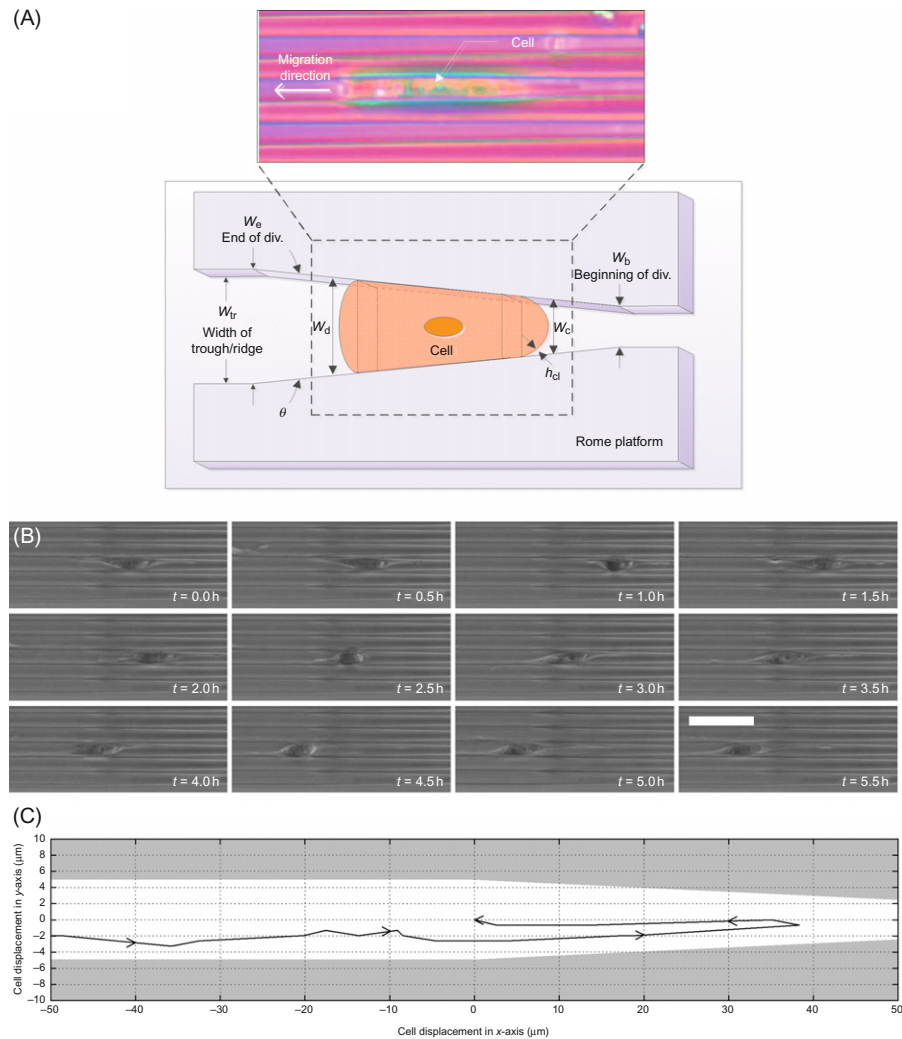
f0015 **FIGURE 5.2**

Passive control of cell (NIH 3T3 fibroblasts) movement using the Rome platform. (A) Cell movement guided by the Rome platform. An adherent cell changes its morphological shape along the troughs and ridges of the diverging micropatterns. The change in cell morphology on the Rome platform, similar to that of *in vivo* cell movement, makes the cell move in the diverging direction of the diverging micropatterns. (B) ~~Optical sequential~~ images showing the migratory behavior of NIH 3T3 fibroblasts on the diverging micropatterns. Even when an adherent cell starts to move in the opposite direction (converging direction of the diverging micropatterns), the diverging micropatterns compel the cell to move in the diverging direction. (C) Movement path of the cell obtained from the ~~optical sequential~~ images of (B). Scale bar of (B) is 50 μm.

where η is a fluid viscosity [44]. The ratio of fluidic resistance in a diverging direction to that in a converging direction, Ω_d/Ω_c, is written as

$$\frac{\Omega_d}{\Omega_c} = \frac{w_c}{w_d} \left\{ \frac{1 - \sum_{n=1,3,5,\ldots}^{\infty} (1/n^5)(192/\pi^5)(h_{cl}/w_c)\tan h(n\pi w_c/2h_{cl})}{1 - \sum_{n=1,3,5,\ldots}^{\infty} (1/n^5)(192/\pi^5)(h_{cl}/w_d)\tan h(n\pi w_d/2h_{cl})} \right\} \approx \frac{w_c}{w_d} < 1$$

$$(5.2)$$

where w_c and w_d are the widths of the leading and the trailing edges with a height of h_{cl}, respectively. The calculated ratio is less than 1, meaning cell movement in a diverging direction has less energy loss caused by fluidic resistance than that in a converging direction. Thus, adherent cells located on a diverging micropattern move in a diverging direction of the diverging micropattern, rather than in a converging direction.

5.2.2 Materials and methods

5.2.2.1 Microfabrication

The fabrication of the Rome platform started by making a reusable master mold on a silicon (Si) wafer. A 4 in (500 μm thick) Si wafer was cleaned with a piranha solution of 1:1 v—v, 96% sulfuric acid (H_2SO_4) and 30% hydrogen peroxide (H_2O_2) for 10 min. To prepare a master mold, 3 μm thick photoresist (SU-8 2002, MicroChem Corp.) was spin-coated at 1000 rpm for 30 s, followed by soft baking at 95°C for 2 min, exposure at 135 mJ/cm^2, postexposure baking at 95°C for 2 min, and developing with an organic solvent solution (SU-8 developer, MicroChem Corp., Figure 5.3A). A polydimethylsiloxane (PDMS, MicroChem Corp.) stamp was fabricated by pouring PDMS over the SU-8 master, curing at 65°C for 2 h, and peeling off from the SU-8 master mold (Figure 5.3B). A photo-curable hybrid polymer substrate (ORMOCER, MicroChem Corp.) was prepared through spin-coating (2000 rpm, 30 s) and ultraviolet (UV) curing (300 mJ/cm^2 at 365 nm wavelength) of 2 ml of ORMOCER resin on a 150 μm thick microscope cover glass that was pretreated with an oxygen plasma chamber (PM-100 Plasma Treatment System, March Plasma Systems, Inc.) at 100 W for 30 s (Figure 5.3C). After additional spin-coating of 1 ml of ORMOCER resin and prebaking at 80°C for 2 min, the PDMS stamp was imprinted on the ORMOCER layer to transfer diverging micropatterns (Figure 5.3D). This ORMOCER substrate was UV cured (Figure 5.3E), followed by demolding and hard baking at 150°C for 1 h (Figure 5.3F).

The fabricated assay was transparent in the visual spectrum (Figure 5.3G). Our assay consisted of parallel and narrow troughs (zone I), diverging troughs (zone II), and parallel and wide troughs (zone III). Five kinds of 3 μm thick assays (Figure 5.3H) have different divergence angles, θ, of 0.5, 1.0, 2.0, 4.0, and 5.0° in the zone II, a narrow width of trough (beginning of divergence), w_b, of
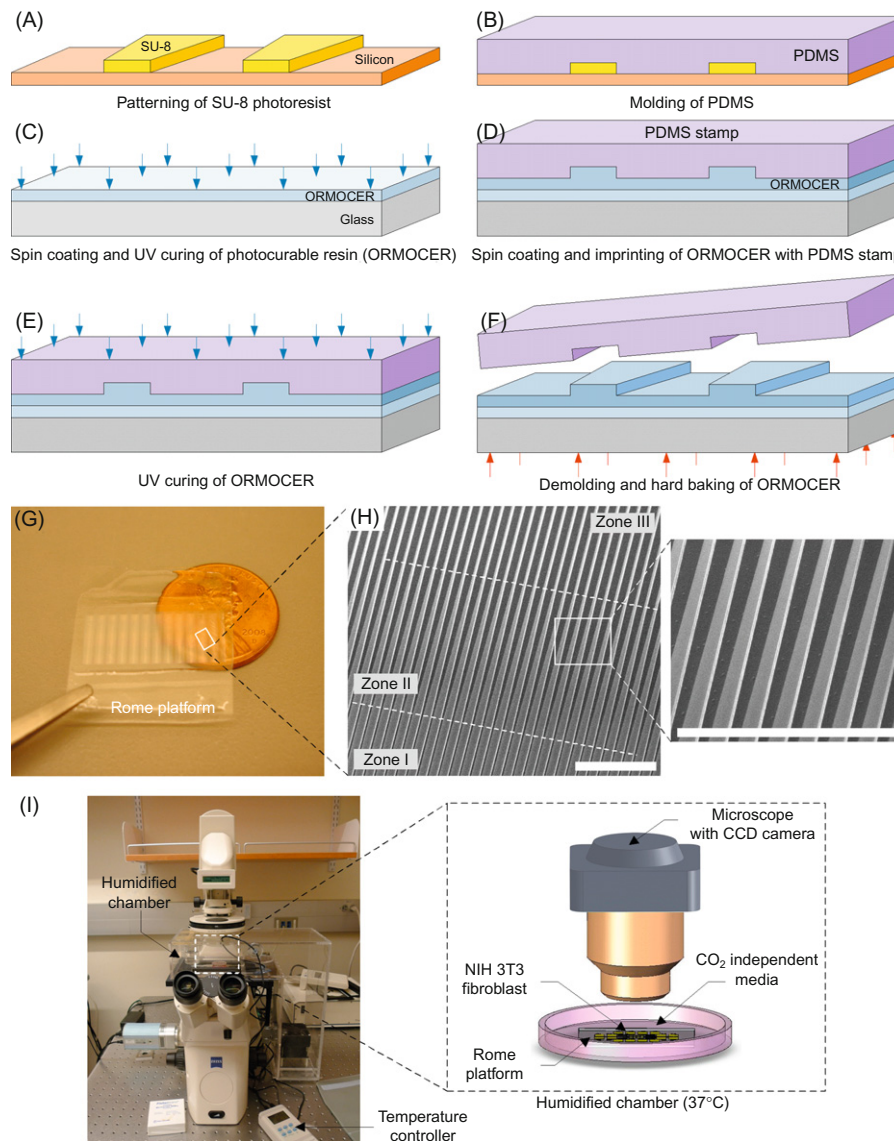
f0020 **FIGURE 5.3**

Microfabrication and experimental setup of the Rome platform. (A–F) Fabrication process: patterning of SU-8 photoresist on a 4 in silicon wafer to prepare a master for PDMS molding (A); PDMS molding to fabricate a reusable PDMS stamp (B); first spin-coating and UV curing of ORMOCER resin on a microscope cover glass to fabricate the substrate of the Rome platform (C); second spin coating of ORMOCER resin, followed by

AU:9

(*Continued*)

$3 \, \mu m$ in the zone I, and a wide width of trough (end of divergence), w_e, of $10 \, \mu m$ in the zone III.

s0035 ### 5.2.2.2 Cell culture

p0070 NIH 3T3 mouse embryonic fibroblast cells (NIH 3T3 fibroblasts) were cultured in a Dulbecco's modified eagle medium (DMEM, GIBCO™) supplemented with 10% fetal bovine serum (FBS, GIBCO™) and 1% Penicillin−Streptomycin (Pen/Strep, GIBCO™) at 37°C in a humidified atmosphere of 5% CO_2. Cells were passaged every 5 days as follows. The cells were washed once in a $1\times$ phosphate buffered saline (PBS, Sigma-Aldrich) solution and then trypsinized with a 0.5% Trypsin−EDTA solution (Sigma-Aldrich). After centrifuging the cells, they were inoculated into a new petri dish. NIH 3T3 fibroblasts with a passage number of 10−20 were used in our experiments. Before each experiment, the fabricated assay was sterilized with 70% ethanol, washed twice with a $1\times$ PBS solution, and incubated with a CO_2 independent medium (GIBCO™) supplemented with 10% FBS and 1% Pen/Strep for 1 h at room temperature. The assay was placed in a petri dish containing a 5 ml CO_2 independent medium with a cell suspension of about 1×10^4 cells/ml. After 1 h of cell seeding, unadhered cells were removed by washing in a $1\times$ PBS solution, followed by replacement with a fresh CO_2 independent medium (10% FBS and 1% Pen/Strep). All experiments were carried out after 24 h of cell seeding at 37°C in a humidified chamber.

s0040 ### 5.2.2.3 Confocal immunofluorescence microscopy

p0075 The state of contact of NIH 3T3 fibroblasts to diverging micropatterns was assessed from immunofluorescence images (Figure 5.4F). Cells were fixed with a 4% (v/v) formaldehyde (Fisher Scientific) diluted with chilled $1\times$ PBS solution for 15 min. The fixed cells were permeabilized with a $200 \, \mu l$ 0.5% (v/v) Triton X-100 (Sigma-Aldrich) diluted with $1\times$ PBS solution at room temperature for 10 min and then were washed three times with a $1\times$ PBS solution, followed by blocking nonspecific binding using a 3% (w/v) nonfat dry milk (Cell Signaling Technology, Inc.) diluted with $1\times$ PBS solution at 4°C for 1 h and washing the cells once with a $1\times$ PBS solution. A $10 \, \mu l$ methanolic stock solution of rhodamine phalloidin (Biotium, Inc.) was diluted with a $200 \, \mu l$ $1\times$ PBS solution

◀ imprinting with the PDMS stamp to define micropatterns (D); second UV curing (E); demolding and hard baking (F). (G and H) Microfabricated assay. Optical photograph of the assay placed on top of a one-cent coin, showing its transparency (G); scanning electron microscopy (SEM) images of the assay (H). (I) Experimental setup. NIH 3T3 fibroblasts are loaded on the assay at 37°C in a CO_2 independent media supplemented with 10% FBS and 1% Pen/Strep. The migratory behavior of the cells is monitored with an inverted microscope equipped with a charge-coupled device (CCD) camera to obtain their sequential images. Scale bars of (H) are $100 \, \mu m$.
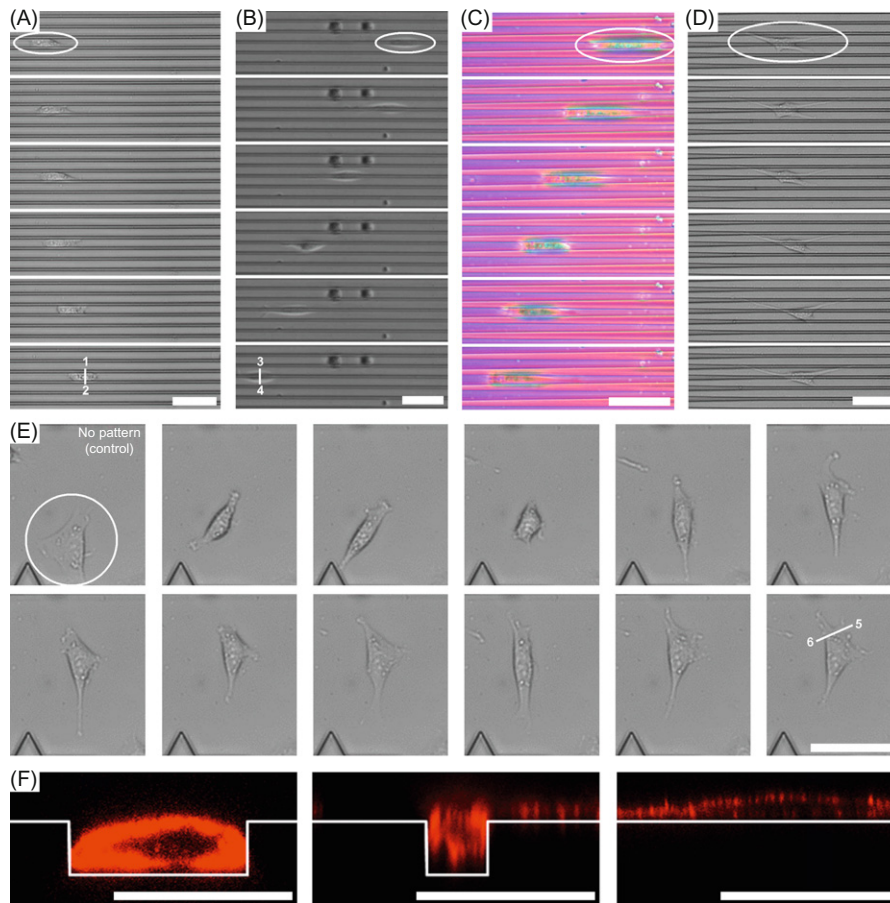
f0025

FIGURE 5.4

Optical ~~sequential~~ and confocal images of NIH 3T3 fibroblasts moving on the Rome platform. (A) Guided cell movement along a single parallel and wide trough (zone III). (B) Guided cell movement along a single parallel and narrow trough (zone I). (C) Guided cell movement along a single diverging trough (zone II). (D) Guided cell movement along multiple (more than two) micropatterns. (E) Unguided cell movement on a flat substrate with no topographical feature (control group). All images of (A–E) are taken every 30 min 24 h after cell loading. (F) Confocal images of the cells placed on the zone III (left, along line 1–2 of (A)), on the zone I (center, along line 3–4 of (B)), and on the flat substrate (right, along line 5–6 of (E)). The actin filaments of the cells were stained with rhodamine phalloidin (red) for immunofluorescence imaging. The confocal images show the cells contact to both two sides of the trough and bottom substrate. Scale bars of (A–E) are 50 μm and those of (F) are 10 μm. (For interpretation of the references to color in this figure legend, the reader is referred to the web version of this book.)

supplemented with 1% Bovine Serum Albumin (Fisher Scientific) for each immunofluorescence staining. The actin filaments of the cells were stained by incubating the cells with this solution for 20 min at room temperature and then washing three times with a 1× PBS solution. Confocal immunofluorescence images were obtained with a confocal laser scanning microscope (LSM 510, Carl Zeiss MicroImaging, Inc.).

s0045 ### 5.2.2.4 Time-lapse microscopy

p0080 The migratory behavior of NIH 3T3 fibroblasts on the Rome platform was monitored with an inverted microscope (Axio Observer A1, Carl Zeiss MicroImaging, Inc.) equipped with a CCD digital camera (Retiga-SRV, QImaging; Figure 5.3I). The location of each cell was automatically tracked every 30 min interval for 24 h using an imaging and analysis tool (QCapture PRO 5, QImaging). At least 10 migrating cells, isolated from each other, were selected for statistical analysis in each experiment, thus obtaining 48 images for each cell—total 480 images from each experiment. Our experiments were conducted at least 10 times for each assay. The movement path of each cell was tracked from the obtained time-sequential images. In detail, after identifying a cell of interest, the coordinates of the cell (especially, nucleus) were obtained by analyzing the time-sequential images and then the relative displacement of the cell at each time interval was calculated.

s0050 ### 5.2.2.5 Analysis of cell motility

p0085 Cell motility speed, s, and cell motility angle, ϕ, were analyzed to characterize the migratory behavior of NIH 3T3 fibroblasts. Cell motility speed and cell motility angle at each time interval, Δt, were calculated from the relative displacement, δx and δy, of each cell.

$$s = \sqrt{\left(\frac{\delta x}{\Delta t}\right)^2 + \left(\frac{\delta y}{\Delta t}\right)^2} \tag{5.3}$$

$$\phi = \arctan\left(\frac{\delta y}{\delta x}\right) \tag{5.4}$$

p0090 Cell motility angle is between 0° and 90°, where 0° represents a direction along micropatterns (x-axis direction) and 90° means a direction across them (y-axis direction). Cell movement on a flat substrate with no topographic feature therefore has a cell motility angle of about 45° [24].

p0095 The migratory behavior of NIH 3T3 fibroblasts migrating on the Rome platform was also quantified by fitting the mean-squared displacement, $\langle d^2(t)\rangle$, of the cells to a persistent random walk model. This mean-squared displacement was obtained from the location data of the cells over entire experiment time, ultimately yielding the directional persistence time and random motility coefficient of each cell. When calculating the mean-squared displacement, we used an

overlapping time interval sampling method (e.g., $0-1$, $0.5-1.5$, and $1-2$ h) over a time interval of $i\Delta t$ larger than the smallest time interval (i.e., 30 min). All mean-squared displacements were averaged as follows:

$$\langle d^2(t)\rangle = \frac{1}{N-i+1}\sum_{k=0}^{N-i+1}[\{x((k+i)\Delta t)-x(k\Delta t)\}^2 + \{y((k+i)\Delta t)-y(k\Delta t)\}^2] \quad (5.5)$$

where N is the total number of time intervals over all experiment time and x and y are the coordinates of the cell at each time interval [45]. This equation yielded a series of $\langle d^2(t)\rangle$ for increasing time interval value, $i\Delta t$. Directional persistence time and random motility coefficient were found by fitting the mean-squared displacement calculated from experimental data to a theoretical mean-squared displacement [45−48].

$$\langle d^2(t)\rangle = 2n_{\mathrm{d}}\mu\{t - P(1 - \bar{\mathrm{e}}^{-t/P})\} \quad (5.6)$$

where n_{d} is a number of dimensions tracked in the experiments (i.e., $n_{\mathrm{d}} = 2$ in our analysis), μ is a random motility coefficient defined as $\mu = s^2 P/n_{\mathrm{d}}$ [46], and P is a directional persistence time. The random motility coefficient can be interpreted as a diffusional representation of moving cell distribution, while the cell motility speed indicates a simple rate of cell movement. The directional persistence time means an average length of time between significant changes in a direction of cell movement along micropatterns. The values of P and μ for cells moving on the Rome platform were obtained from experimental data corresponding to one-third of total cell movement because the true movement path of cells was unable to be monitored for enough time [49]. Some cells whose measured mean-squared displacement showed much discrepancy from theoretical mean-squared displacement were not considered in this analysis.

p0100 Statistical analysis was made using a commercial statistical tool (Minitab 14, Minitab, Inc.) to quantify the migratory behavior of adherent cells (e.g., cell motility speed, cell motility angle, directional persistence time, and random motility coefficient). Each measurement result was analyzed using one-way analysis of variance (ANOVA) with Bonferroni *post hoc* test. P-values less than or equal to 0.05 were considered statistically significant. All data were represented as mean ± standard error (of the mean) values.

s0055 ## 5.2.3 Results and discussion

s0060 ### 5.2.3.1 Effect of micropatterns on cell motility

p0105 The effect of the dimensions and shape of micropatterns on cell motility was characterized. The movement of NIH 3T3 fibroblasts on a variety of substrates with different micropatterns was compared to that of the cells on a flat substrate. The nucleus location of each NIH 3T3 fibroblast, seeded on each substrate, was recorded every 30 min for 24 h using time-lapse microscopy (Figure 5.4A−E).

Continuous movement paths of at least five cells of each substrate were obtained by analyzing the measured cell location (Figure 5.5A−F).

p0110   NIH 3T3 fibroblasts on a flat substrate (control group, Figures 5.4E and 5.5F) had randomly oriented protrusions and freely moved without any directionality in their movement. The percentage for cells which moved within sectors of −22.5° to 22.5° and 157.5 to 202.5° was 24.1%, and the percentage for cells which traveled within sectors of 67.5−112.5° and 247.5−292.5° was 25.9% where 0° meant a positive x-axis direction.

p0115   The cells, seeded on parallel micropatterns with different widths of trough/ridge of 3 and 10 µm, moved along the micropatterns. In the parallel micropatterns with a width of trough/ridge of 10 µm (Figure 5.4A), 75.9% and 60.3% of the cells migrated along troughs and ridges, respectively, while 5.2% and 12.6% of the cells moved across troughs and ridges, respectively. Here, "along troughs and ridges" means sectors of −22.5° to 22.5° and 157.5 to 202.5° and "across troughs and ridges" indicates sectors of 67.5−112.5° and 247.5−292.5° where the direction of the parallel micropatterns is set as 0°. In the parallel micropatterns
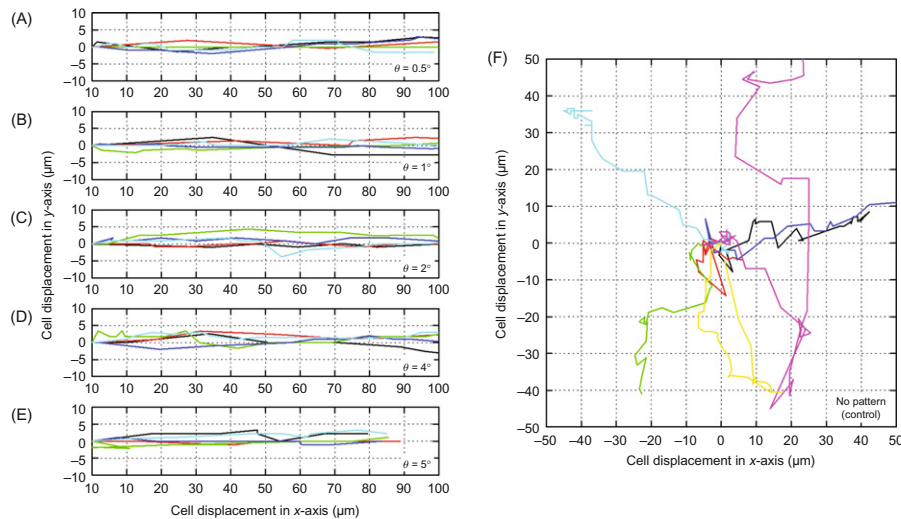
FIGURE 5.5

f0030

Movement paths of NIH 3T3 fibroblasts migrating on the Rome platform. The paths connect the positions of each cell (especially, nucleus) every 30 min, thus showing the trajectory of each cell which moves on the Rome platform. (A−E) Measured movement paths of the cells along diverging micropatterns with different divergence angles of 0.5° (A), 1.0° (B), 2.0° (C), 4.0° (D), and 5.0° (E). (F) Measured movement paths of the cells migrating on a flat substrate with no topographical feature (control group). The guided cell motility paths (A−E) are compared to the unguided ones (F).

with a width of trough/ridge of 3 μm (Figure 5.4B), average percentages for cells which traveled along troughs and ridges were 79.8% and 61.2%, respectively, whereas average percentages for cells which moved across troughs and ridges were only 4.4% and 11.8%, respectively. These results let us know the following biological facts. First of all, adherent cells tend to move along parallel micropatterns rather than across parallel micropatterns. When adherent cells sense the physical cues (e.g., troughs and ridges) of the parallel micropatterns, the cells start to stretch themselves along the micropatterns to maximize their contact area to the physical cues (Figure 5.4F). This change in cell morphology results in guided cell movement along the micropatterns. Secondly, this tendency is in inverse proportion to the width of trough/ridge, showing that the degree of change in cell morphology by micropatterns is correlated to the direction of cell movement.

p0120   In the diverging micropatterns with different divergence angles of 0.5°, 1.0°, 2.0°, 4.0°, and 5.0° (Figures 5.4C and 5.5A−E), the movement of NIH 3T3 fibroblasts was also well-guided along the micropatterns. On average, 76.4% and 72.1% of the cells traveled along the troughs and ridges of the diverging micropatterns, respectively, and 4.6% and 7.6% of the cells moved across the troughs and ridges, respectively. The percentage for cells which travel along troughs and ridges increased as the divergence angle of the diverging micropatterns increased. This suggests that the micropatterns with a larger divergence angle can lead to a relatively sudden change in cell morphology, compared to the micropatterns with a smaller divergence angle, which positively affects cell movement along the micropatterns.

s0065 5.2.3.2 Effect of micropatterns on migratory characteristics of adherent cells

p0125 We also characterized the effect of the dimensions and shape of diverging micropatterns on cell migratory characteristics such as cell motility speed, cell motility angle, directional persistence time, and random motility coefficient. The cell motility speed was used to quantify the rate at which cells migrate; the cell motility angle was measured to indicate the movement direction of adherent cells; the directional persistence time was calculated to gage how long the diverging micropatterns maintain cell movement without significant changes in the movement direction of NIH 3T3 fibroblasts; the random motility coefficient was computed to explore how the cells disperse on the diverging micropattern. The cell migratory characteristics were determined by modeling the measured movement paths of the cells (Figure 5.5) as a persistent random walk model [45−48]. As diverging micropatterns were fully described by three parameters (w_b, w_e, and θ, where w_b and w_e are two widths of trough/ridge at which the divergence of diverging micropatterns begins and ends, respectively, and θ is a divergence angle; see Figure 5.2A), the effects of both two widths of trough/ridge and divergence angle on the migratory characteristics of adherent cells were independently quantified.

s0070 ## Dependence of cell migratory characteristics on width of trough/ridge

p0130 First of all, the effect of the width of trough/ridge of micropatterns on cell motility speed was explored using our assay (Figure 5.6A). The cell motility speed, s, calculated from Eq. (5.2) had an inverse relation to the width of trough/ridge, w_{tr}, represented as s (μm/min) $= 0.26 + 0.88/w_{tr}$ (μm). This can be explained by the following biological phenomena. Assuming no volume change in adherent cells during cell movement, the cells moving on the micropatterns with a narrow width of trough/ridge have a longer displacement per each movement cycle than those traveling on the micropatterns with a wide one. Moreover, the micropatterns with a narrow width of trough/ridge (3 μm in this study) are known to weaken the strength of cell−substrate adhesion slightly, thus maximizing cell motility speed [47]. The motility speed of the cell moving on the micropatterns with a width of trough/ridge of 45.5 ± 3.5 μm was identical to that of the cell migrating on a flat substrate (control group), indicating the micropatterns with a width of trough/ridge larger than 45.5 ± 3.5 μm were recognized as a flat substrate by the cells. This demonstrates that the ceiling and floor values for the width of trough/ridge of the micropatterns which are designed to passively control the motility of NIH 3T3 fibroblasts are 3 μm or less and about 42−49 μm, respectively. Remarkably, when NIH 3T3 fibroblasts were guided by multiple (more than one), identical micropatterns (denoted with an asterisk symbol in Figure 5.6), the motility speed of the cells was determined by the largest dimension of the micropatterns to which the circumferential marginal zone of the cells contacted (see Figure 5.4D). This suggests that cell mechanosensors which receive and respond to external physical cues (e.g., micropatterns in this study) are intensively activated at the circumferential marginal zone of the cell rather than at the central zone.

p0135 The dependence of cell motility angle on the width of trough/ridge was also explored by analyzing the measured movement paths of NIH 3T3 fibroblasts (Figure 5.6B). The cell motility angle, calculated using Eq. (5.3), was proportional to the width of trough/ridge, and the cell motility angle obtained from the micropatterns was much smaller than that of a control group. This shows that the micropatterns with a narrow width of trough/ridge are helpful to achieve directed cell movement.

p0140 In contrast to the cell motility speed, the directional persistence time got maximized at a width of trough/ridge of 10 μm (Figure 5.6C). That is, the directional persistence time evidently decreased on the micropatterns with narrow (3 μm) and wide (24.5 μm) widths of trough/ridge. The NIH 3T3 fibroblasts on the micropatterns with a narrow width of trough/ridge seem to easily escape from the micropatterns and to sense other topographical features around the micropatterns due to a relatively small contact area to the micropatterns, whereas the cells on the micropatterns with a wide width of trough/ridge are thought to incompletely sense the micropatterns. This indicates the width of trough/ridge of 10 μm, comparable to the size of NIH 3T3 fibroblasts, can prevent the cells from frequently
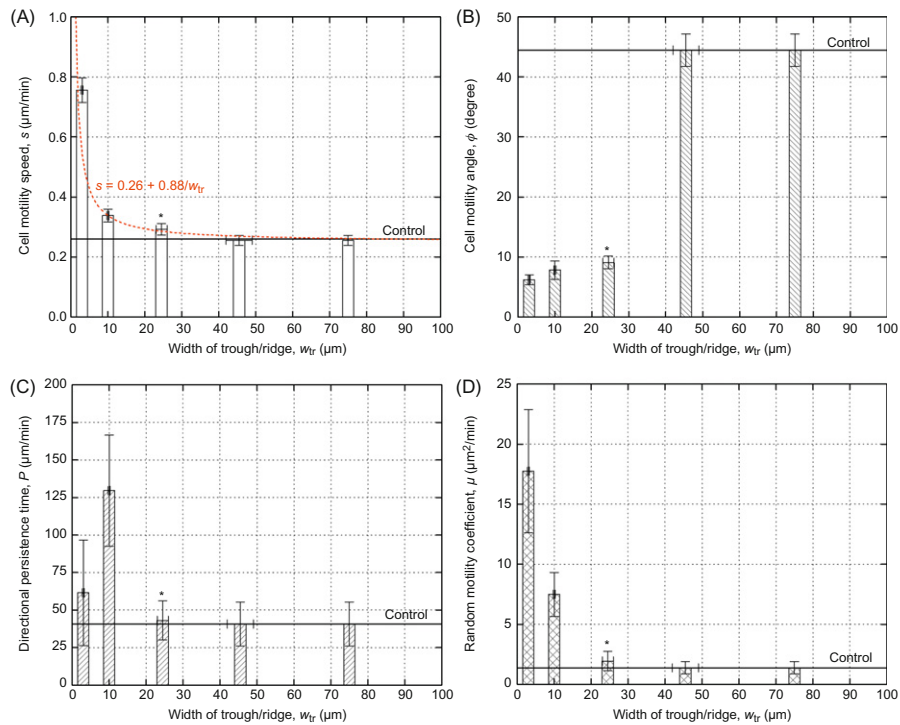
f0035

FIGURE 5.6

Quantification of the migratory behavior of NIH 3T3 fibroblasts in response to (parallel) micropatterns with different widths of trough/ridge. (A) Cell motility speed, s (μm/min), as a function of the width of trough/ridge of micropatterns, w_c (μm). The measured cell motility speed decreases as the width of trough/ridge increases, expressed as $s = 0.26 + 0.88/w_c$. This result suggests that there are both ceiling and floor values for the dimensions of micropatterns which can influence cell movement, and the ceiling and floor values of NIH 3T3 fibroblasts are 3 μm (or less) and about 42–49 μm, respectively. (B) Cell motility angle as a function of the width of trough/ridge of micropatterns. The measured cell motility angle is proportional to the width of trough/ridge, w_c, at $w_c \leq 45.5 \pm 3.5$ μm but is the same as that of a control group at $w_c > 45.5 \pm 3.5$ μm. (C) Directional persistence time as a function of the width of trough/ridge of micropatterns. The directional persistence time of NIH 3T3 fibroblasts is maximized when the width of trough/ridge is about 10 μm. (D) Random motility coefficient as a function of the width of trough/ridge of micropatterns. The measured random motility coefficient is in inverse proportion to the pitch of ridges, which is explained in Figure 5.7A. The symbol of asterisk denotes the cells moving on multiple, identical micropatterns. All results are compared with the migratory characteristics of a control group. Error bars of (A–D) are the standard errors of the means.

changing their movement direction, thus forcing the cells to move in a specified direction for a relatively long time.

p0145   The random motility coefficient was also calculated as a function of the width of trough/ridge (Figure 5.6D). The calculated random motility coefficient was inversely proportional to the width of trough/ridge of micropatterns, like the cell motility speed. In other words, the amount of the cells moving across a unit area through a unit structural nonuniformity in a unit time decreased as the width of trough/ridge of micropatterns increased. Although micropatterns with 3 μm width of trough/ridge did not have the longest directional persistence time, the random motility coefficient of the micropatterns was highest. This is because the random motility coefficient is also related to the cell motility speed (Figure 5.6A) that significantly increases as the width of trough/ridge of micropatterns decreases. The random motility coefficient of the cell moving on the micropatterns with a width of trough/ridge of 45.5 μm was also the same as that of a control group.

p0150   Together with the experimental results of cell motility speed and cell motility angle (Figure 5.6A, B), we conclude as follows. Micropatterns with a narrow width of trough/ridge are of assistance to achieve fast, one-directional, and large-amount cell movement although they sacrifice the directional persistence time. When adherent cells need to be guided for a long time, the width of trough/ridge of the micropatterns must be comparable to the size of the cells (e.g., about 10 μm for NIH 3T3 fibroblasts). Two widths of trough/ridge of the diverging micropatterns which control the motility of NIH 3T3 fibroblasts need to be in the range of 3−24.5 μm (less than 45.5 μm).

s0075 ## Dependence of cell migratory characteristics on divergence angle

p0155 The effect of the divergence angle of diverging micropatterns on the cell motility speed, cell motility angle, directional persistence time, and random motility coefficient of NIH 3T3 fibroblasts was investigated using the Rome platform. The cell motility speed was characterized as a function of the divergence angle of diverging micropatterns (Figure 5.7A). Although the diverging micropatterns prominently enhanced the cell motility speed, compared to that on a flat substrate (control group), the measured cell motility speed was almost insensitive to the divergence angle. Together with the dependence of cell motility speed on the width of trough/ridge of parallel micropatterns (see Figure 5.6A), the motility speed of adherent cells that contact to diverging micropatterns can be controlled by adjusting two widths of trough/ridge of diverging micropatterns at which divergence begins and ends, respectively. This result points out how to design the diverging micropatterns for the control of cell motility. Like cell movement on the parallel micropatterns, the cells on the troughs of the diverging micropatterns moved slightly faster than the cells on the ridges. The reason for this behavior seems that the troughs offer higher stability in maintaining cell movement than the ridges.

p0160   We also quantified the dependence of cell motility angle on the divergence angle of diverging micropatterns (Figure 5.7B). The cell motility angle was much smaller than that of a control group; the measured cell motility angle was in direct
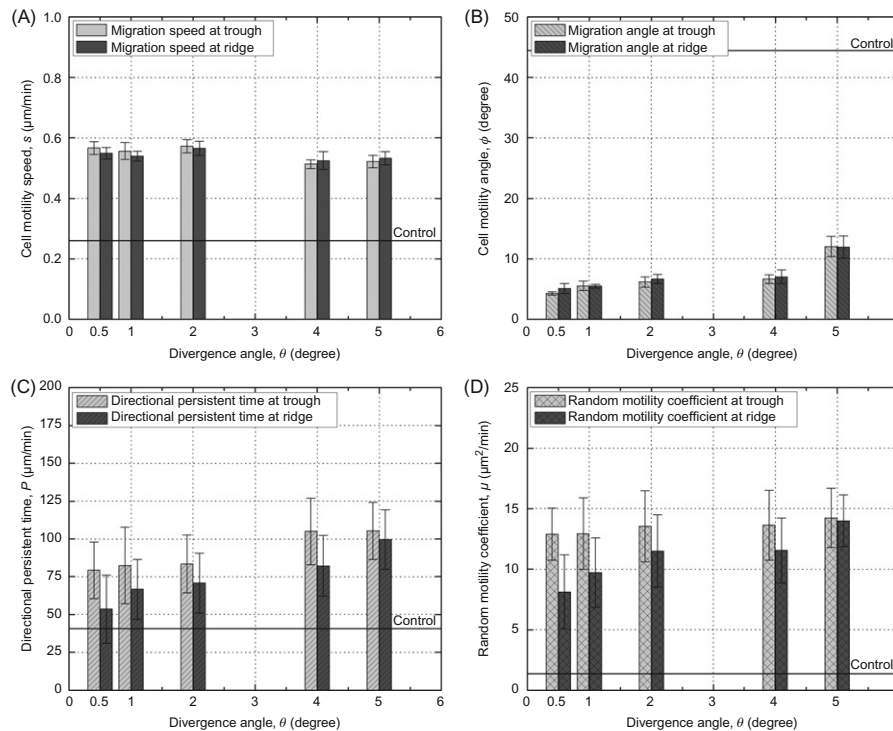
f0040 **FIGURE 5.7**

Quantification of the migratory behavior of NIH 3T3 fibroblasts using diverging micropatterns with different divergence angles. (A) Cell motility speed as a function of the divergence angle of diverging micropatterns. All diverging micropatterns are identical in their two widths of trough/ridge (w_w and w_n) at which divergence begins and ends, respectively. This shows cell motility speed is almost insensitive to the divergence angle. Compared to a flat substrate, the troughs of the diverging micropatterns expedite cell movement slightly (not prominently) more than the ridges. This indicates that the migratory behavior of adherent cells can be controlled by both troughs and ridges, but the troughs are more effective. (B) Cell motility angle as a function of the divergence angle of diverging micropatterns, showing the diverging micropatterns, have a capability to force adherent cells to move in one direction. The measured cell motility angle is in direct proportion to the divergence angle. (C) Directional persistence time as a function of the divergence angle of diverging micropatterns. The measured directional persistence time is also proportional to the divergence angle. The directional persistence time obtained from the cells moving on the troughs is larger than that obtained from the cells traveling on the ridges because the cells tend to move from the ridges to the troughs more than the opposite. (D) Random motility coefficient as a function of the divergence angle of diverging micropatterns. All quantification results show that the diverging micropatterns can control the direction and rate of cell movement in a passive way, and the troughs of the diverging micropatterns are more effective to control cell movement than the ridges. All results are compared with the migratory characteristics of a control group. Error bars of (A−D) are the standard errors of the means.

proportion to the divergence angle; the trough and ridges have no prominent difference in cell motility angle. These measurements show that the diverging micropatterns with a large-divergence angle impose a relatively high-level morphological polarity on adherent cells, compared to those with a small-divergence angle, which makes the cells deviate a little from their designated course within a reasonable range (not randomly). However, this behavior never affects the controllability of diverging micropatterns which determines the movement direction of adherent cells.

p0165   Next, the directional persistence time was measured as a function of the divergence angle (Figure 5.7C). The increase in the divergence angle contributed to increase the directional persistence time; the cell moving on the troughs had a longer directional persistence time than the cells moving on the ridges. The former is due to the relatively high morphological polarity caused by the diverging micropatterns with a large-divergence angle. Namely, the cells guided by diverging micropatterns with a large-divergence angle have blunter leading edge and sharper trailing edge than those guided by diverging micropatterns with a small-divergence angle, thus maintaining the direction of cell movement (without significant changes) for a longer time. The latter is because the troughs make the cells straightly move for a longer time (by using their upward sides) than the ridges. These results suggest that the diverging micropatterns with a large-divergence angle are preferable to control cell movement in a designated direction for a long time, although they have an acceptable loss in manipulating the direction of cell movement.

p0170   The random motility coefficient of the NIH 3T3 fibroblasts moving on the diverging micropatterns was plotted as a function of the divergence angle of diverging micropatterns (Figure 5.7D). The obtained random motility coefficient was proportional to the divergence angle; the cells moving on the troughs of the diverging micropatterns had a higher random motility coefficient than those moving on the ridges. These let us know the level of morphological polarity, determined by the divergence angle of the diverging micropatterns, has a correlation with random motility coefficient.

AU:1

p0175   All migratory characteristics (Figure 5.7A−D), obtained from NIH 3T3 fibroblasts moving on the diverging micropatterns, reveal the following facts: (i) in contrast to parallel micropatterns which guide adherent cells from right to left or vice versa along them, diverging micropatterns make adherent cells to move in a specified direction (i.e., diverging direction of the micropatterns), thus effectively controlling the movement direction of the cells; (ii) when adherent cells are guided using diverging micropatterns, the movement speed of the cells is determined not by the divergence angle of the diverging micropatterns but by the width of trough/ridge (i.e., two widths of trough/ridge where divergence begins and ends, respectively); (iii) the motility angle, directional persistence time, and random motility coefficient of adherent cells can be effectively controlled by adjusting the divergence angle of diverging micropatterns, which yields useful propositions for the design of diverging micropatterns which are intended to control cell motility.

s0080 **5.3 Active control of cell motility**

s0085 **5.3.1 Biological breadboard**

p0180 A BBB consists of identical gold electrodes patterned on a Pyrex substrate, which entitles this platform to a high degree-of-freedom in manipulating cell detachment at a subcellular level (Figure 5.8A). The Pyrex substrate and gold electrodes are modified with polyethylene glycol (PEG) and RGD-terminated thiol (RTT), respectively. The RTT modification is intended to make the gold electrodes cell-adhesive by tethering an RGD peptide to a gold surface via thiol compound.
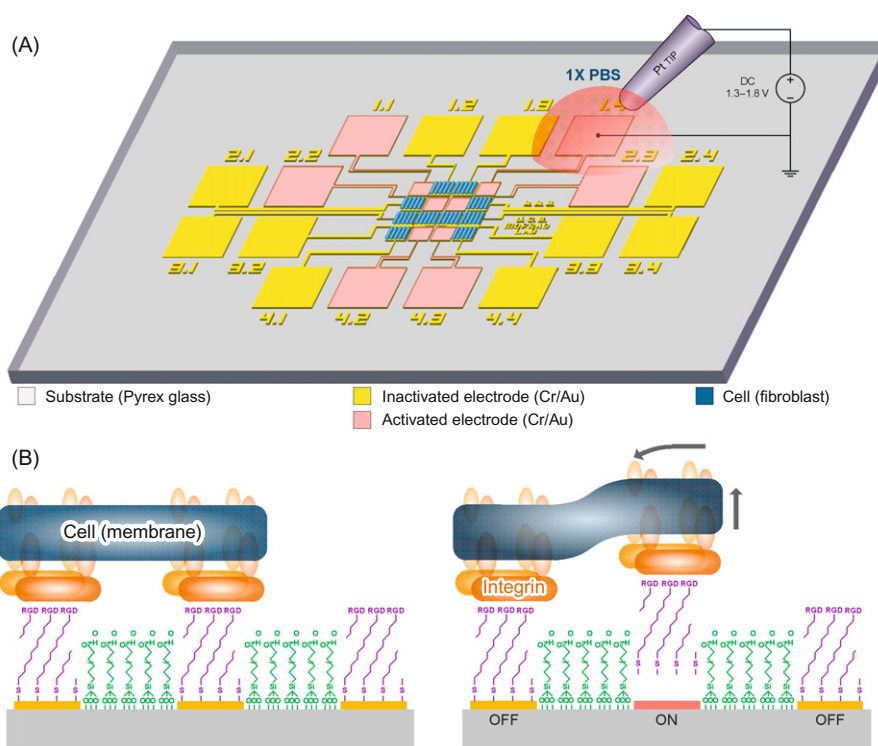
FIGURE 5.8

f0045

A BBB for the active control of cell motility. (A) Schematic of the BBB consisting of gold electrodes patterned on a Pyrex substrate. This platform has the addressability, multifunctionality, and reusability in manipulating cell detachment due to its structure and working principle. (B) Cell detachment manipulation using the BBB. A cell adheres to all gold electrodes functionalized with RTT (left). The cell (or part of the cell) is detached when a target electrode (second one from left) is activated by applying an activation potential which reductively desorbs a gold—thiol SAM.

The thiol compound creates a SAM on the gold electrodes following the spontaneous chemisorption

$$R - S - H + Au \rightarrow R - S - Au + \tfrac{1}{2}H_2 \tag{5.7}$$

where R is a substituent [50]. The RTT therefore offered a cell (strictly speaking, integrin)-binding site which is almost same as *in vivo* microenvironment for cell adhesion. The PEG modification on the Pyrex substrate is designed to achieve a cell-resistive surface where hydrated neutral PEG chains sterically repulse cells.

p0185   In the spatiotemporal manipulation of cell detachment, adherent cells are loaded on the BBB modified with RTT and PEG and then start to stretch on the RGD peptide of the gold electrodes. On the manipulation of cell detachment, the entire cells (or part of the cell) are detached from the BBB by activating gold electrode(s) which breaks a chemical bonding between gold and thiol (Figure 5.8B). When the RTT-modified gold electrodes are activated with activation potential of −0.9 to −1.8 V, a gold−thiol SAM is reductively desorbed [51]

$$R - S - Au + H^+ + e^- \rightarrow R - S - H + Au \tag{5.8}$$
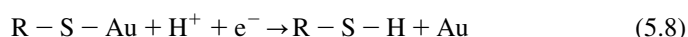
p0190   The detached cells (or part of the cell) sense no external mechanical anchorage (i.e., focal adhesion) to a substrate and are liquefied through the gel−sol transition of their cytoskeleton, followed by cellular retraction.

s0090 ## 5.3.2 Materials and methods

s0095 ### 5.3.2.1 Microfabrication

p0195 The microfabrication of the BBB began with a 500 μm thick, 4 in, Corning 7740 Pyrex glass wafer. After cleaning the wafer in a piranha solution (H_2SO_4: $H_2O_2 = 1:1$), 1 μm thick LOR resist (LOR 10 A, MicroChem Corp.) and 2 μm thick positive photoresist (S1818, Rohm and Haas Corp.) were sequentially spin-coated to prepare a double-layer resist stack for lift-off process. This double-layer resist stack was patterned through lithography (Figure 5.9A, left), followed by the deposition of 5 nm thick chromium (Cr) adhesion layer and 100 nm thick gold (Au) layer through e-beam evaporation (Figure 5.9A, center). Next, the Cr/Au layer was patterned in an organic solvent mixture (BAKER PRS-3000 Stripper, Mallinckrodt Baker, Inc.), thus fabricating two kinds of BBBs (Figure 5.9A, right). One for the manipulation of cell detachment at a cellular level was composed of gold electrodes with a length of 500 μm and a width of 500 μm (Figure 5.9B), the other for the manipulation of cell detachment at a subcellular level consisted of gold lines with a width of 10 μm and a gap of 3 μm (Figure 5.9C). The fabricated BBB was wire-bonded in a chip carrier and then was assembled with a cell-culture-well (Figure 5.9D, left). For the BBB which was used with an inverted microscope, the deposition thickness of the gold layer was reduced to 30 nm to make the BBB transparent (Figure 5.9D, right).
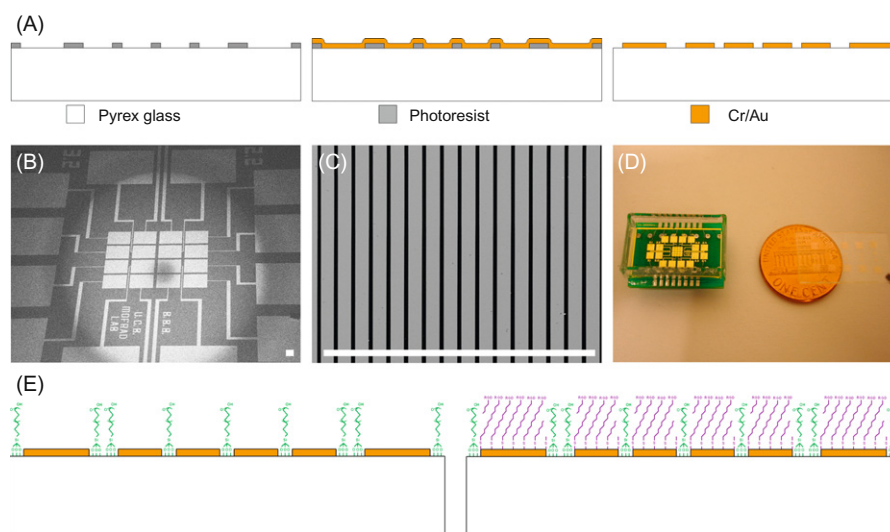
f0050 **FIGURE 5.9**

Microfabrication and surface modifications of the BBB. (A) The BBB is microfabricated by patterning gold electrodes on a Pyrex substrate: patterning of a photoresist layer through lithography (left); deposition of a Cr/Au layer through e-beam evaporation (center); patterning of the deposited Cr/Au layer through lift-off process (right). (B) Microfabricated BBB for the manipulation of cell detachment at a cellular level, each electrode of which is 500 μm in length and 500 μm in width. (C) Microfabricated BBB for the subcellular detachment, each electrode of which is 10 μm in width and 3 μm in gap. (D) Photograph of the BBB before (right) and after (left) assembly, showing its transparency. (E) Surface modification processes of the BBB. The BBB is incubated with a PEG solution to make a Pyrex substrate cell resistive (left) and then it is incubated with a synthesized RTT solution to make gold electrodes cell adhesive (right). Scale bars of (B) and (C) are 100 μm.

s0100 ### 5.3.2.2 PEG modification on Pyrex substrate

p0200 The fabricated BBB was cleaned with an oxygen plasma chamber (PM-100 Plasma Treatment System, March Plasma Systems, Inc.) at 100 W for 30 s. The cleaned BBB was incubated with 2% (v/v) m-PEG silane (Gelest, Inc.) and 1% (v/v) hydrochloric acid (HCl, Fisher Scientific) dissolved in anhydrous toluene (Fisher Scientific) for 2 h (Figure 5.9E, left). This treatment was carried out in a glove box under a nitrogen purge. The incubated BBB was sequentially rinsed in fresh toluene and ethanol, followed by drying with nitrogen and curing at 120°C for 2 h.

s0105 ### 5.3.2.3 RTT functionalization on gold electrodes

p0205 The gold electrodes were functionalized with an RTT solution which was synthesized by chemically combining *cyclo* (Arg-Gly-Asp-D-Phe-Lys) (Peptides

International, Inc.) with dithiobis(succinimidyl undecanoate) (Dojindo Molecular Technologies, Inc.) as follows. The *cyclo* (Arg-Gly-Asp-D-Phe-Lys) was dissolved in dimethoxysulfoxide (DMSO, Sigma-Aldrich) to get 1 mM RGD peptide aliquot and stored at $-20°C$. This reaction was made in a glove box under a nitrogen purge to protect the RGD peptide. The dithiobis(succinimidyl undecanoate) was also prepared in 1 mM aliquot in DMSO and stored at $-20°C$. This preparation was also made in moisture-free environment. When functionalizing the gold electrodes, two aliquots were warmed to room temperature in a desiccator. The RGD peptide aliquot was mixed with 1% (v/v) triethylamine (Fisher Scientific) for 5 min to make all primary amines of a lysine amino acid unprotonated. The same volume of the dithiobis(succinimidyl undecanoate) aliquot was added to the RGD peptide aliquot and then mixed using a vortex mixer for 4 h to synthesize an RTT solution. For the RTT functionalization of the gold electrodes (Figure 5.9E, right), the PEG-treated BBB was incubated with this solution for 1 h at room temperature to promote spontaneous chemisorption between thiol and gold, followed by sonificating in DMSO for 3 min and rinsing in ethanol and PBS (Sigma-Aldrich).

s0110 ### 5.3.2.4 Contact angle measurement

p0210 The contact angles of two surfaces (i.e., PEG-treated Pyrex substrate and RTT-functionalized gold surface) were measured in a sessile drop mode using a goniometer (KRÜSS582, KRÜSS) to characterize the changes in wetting properties of the surfaces through surface modifications. The contact angle of each surface was measured 10 times and then was averaged. The contact angle of PEG-treated Pyrex substrate was compared to that of untreated Pyrex substrate, and the contact angle of RTT-functionalized gold surface was compared to those of untreated gold surface and thiol-treated gold surface.

s0115 ### 5.3.2.5 X-ray photoelectron spectroscopy characterization

p0215 A sample for X-ray photoelectron spectroscopy (XPS) characterization was prepared by performing the RTT functionalization on a Cr/Au layer patterned on a silicon wafer. An untreated gold pattern was run as a control group. The XPS analysis was conducted using a customized ~~ESCA (Omicron NanoTechnology)~~ at   AU:2 1×10^{-8} Torr. All measured spectra were referenced to the position of Au 4f peak. The scans were collected over a range of 20 eV around the peak of interest with a pass energy of 23.5 eV.

s0120 ### 5.3.2.6 Electrochemical characterization of reductive desorption of gold−thiol SAM

p0220 A Cr/Au layer patterned on a silicon wafer was functionalized in the RTT solution to prepare the sample for cyclic voltammetry (CV) characterization. The potentiodynamic electrochemical characterization was performed using a three-electrode system composed of the gold surface of the sample (working electrode), platinum electrode (counter electrode), and Ag/AgCl electrode

(reference electrode). The CV of the reductive desorption of a gold−thiol SAM was measured in Dubecco's phosphate buffered saline (DPBS, Sigma-Aldrich) using a scanning potentiostat (Model 362, EG&G Co.). A scan started cathodically from 0 to −2 V, then annodically back to 0 V at a scan rate of 50 mV/s.

s0125 5.3.2.7 Cell culture

p0225 ~~NIH 3T3 mouse embryonic fibroblast cells~~ (NIH 3T3 fibroblasts~~)~~ were cultured in DMEM (GIBCO™) supplemented with 10% FBS (GIBCO™) and 1% Pen/Strep (GIBCO™) at 37°C in humidified 5% CO_2 atmosphere. The cell was passaged every 4 days. NIH 3T3 fibroblasts with a passage number of 5−20 were used in this study. For each experiment, the surface-modified BBB was sterilized and then was placed on a petri dish containing 5 ml cell-culture medium with a cell suspension of 1×10^6 cells/ml. For subcellular detachment, the cell concentration was changed into 1×10^4 cells/ml. Unadhered cells were removed by washing the BBB in PBS 1 h after cell loading. All experiments were carried out 24 h after cell loading.

s0130 5.3.3 Results and discussion

s0135 5.3.3.1 Surface modifications

p0230 The degree of PEG treatment on Pyrex substrate was verified by both contact angle measurement and cell loading test. The measured contact angle of the PEG-treated Pyrex substrate was $61.5 \pm 3.8°$ on average, while that of untreated Pyrex substrate was $25.7 \pm 1.5°$ (Figure 5.10A). Additionally, NIH 3T3 fibroblasts were seeded on both surfaces and then cell adhesion to each surface was visualized 24 h after cell loading (Figure 5.10B). These results show the PEG treatment makes the Pyrex substrate strongly hydrophobic, thus effectively preventing cell adhesion.

p0235   The RTT functionalization on gold surface was characterized by both contact angle measurement and XPS survey. The average contact angles measured from untreated gold surface, thiol-treated gold surface, and RTT-functionalized gold surface were $67.3 \pm 2.5°$, $53.3 \pm 1.3°$, and $24.6 \pm 2.8°$, respectively (Figure 5.10C). The existence of RGD peptides tethered to the gold electrodes was also investigated using XPS. The measured XPS survey spectrum shows the presence of gold, thiol, and RGD peptides (Figure 5.10D): the peaks of Au 4s, Au 4p, Au 4d, and Au 4f indicate the presence of gold (Au(111)); the peaks of S $2p_{1/2}$ and S $2p_{3/2}$ are corresponding to sulfur from the thiol (right inset); the peaks of C 1s, O 1s, O KLL, and N 1s (left inset) demonstrate there are carbon, oxygen, and nitrogen from the amine ($-NH_2$) and carboxylic ($-COOH$) groups of the RGD peptides. Together with the results of contact angle measurements, this confirms RGD peptides are well linked to the gold electrodes via thiol through RTT functionalization.
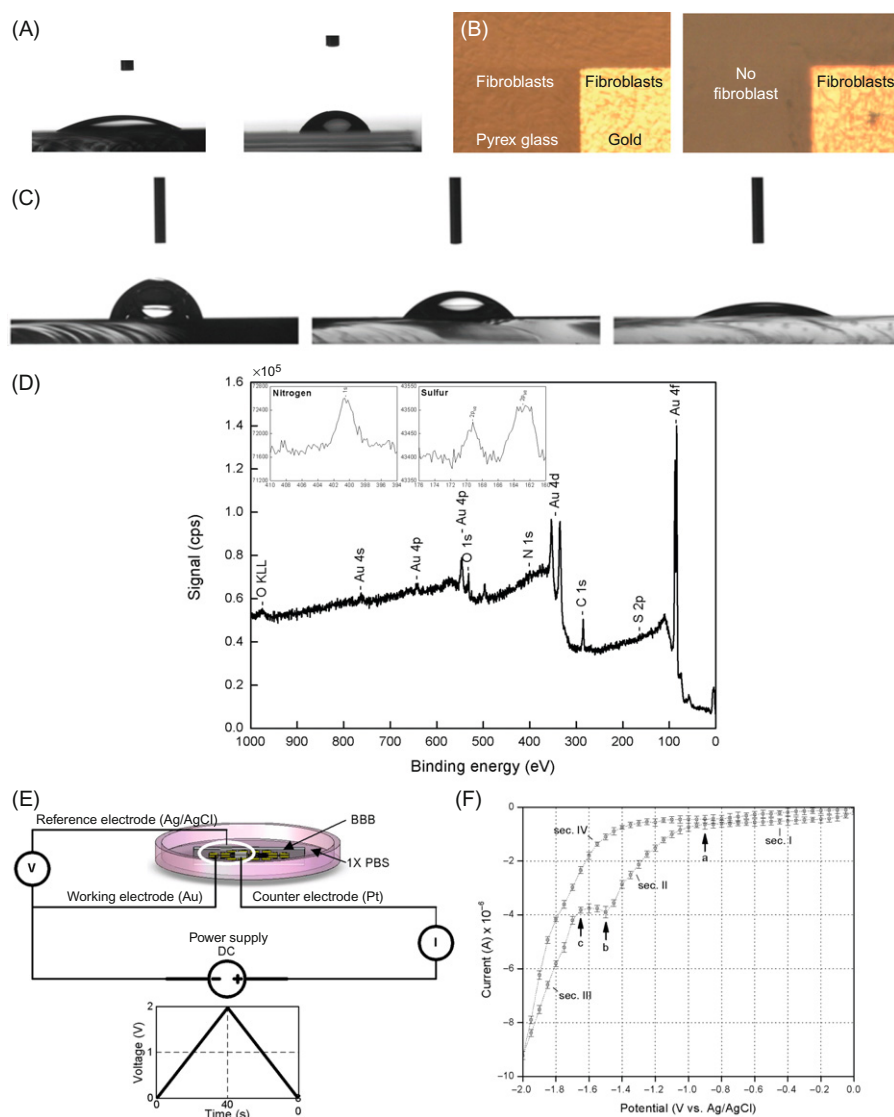
FIGURE 5.10

Characterizations of the surface modifications of the BBB and potentiodynamic electrochemical characterization of the reductive desorption of a gold—thiol SAM.
(A) Contact angles measured from a Pyrex substrate before (left) and after (right) PEG modification. The contact angle is changed from 25.7 ± 1.5° to 61.5 ± 3.8° through PEG modification. (B) Cell (NIH 3T3 fibroblasts) loading on a Pyrex substrate before (left) and after (right) PEG modification, showing the Pyrex substrate is changed from cell adhesive
(*Continued*)

s0140 ### 5.3.3.2 Reductive desorption of gold−thiol SAM

p0240 The reductive desorption of a gold−thiol SAM was verified by measuring CV curves using a three-electrode system (Figure 5.10E). The current at the working electrode (gold electrode of the BBB) was plotted versus the applied voltage with respective to a reference electrode (Figure 5.10F). The part of the CV (sec. I) ranging from 0.00 to −0.90 V was corresponding to no reductive desorption of the SAM; the potential range (sec. II) showed the deductive desorption began and ended at −0.90 V (point a) and −1.65 V (point c), respectively; this electrochemical reaction got maximized at −1.50 V (point b). This measurement shows that the activation potential must be larger than −0.90 V to break the chemical binding between gold and thiol. Considering the generation of hydrogen due to the electrolysis of cell-culture medium at around −2.00 V, the optimum potential for the reductive desorption of a gold−thiol SAM is thought to be −1.00 (larger than −0.90 V) to −1.80 V (less than −2.00 V) at which NIH 3T3 fibroblasts are successfully detached from the gold electrode of the BBB without viability.

s0145 ### 5.3.3.3 Detachment of adherent cells for the control of cell motility

p0245 The spatiotemporal manipulation of cell detachment at a cellular level was characterized by disconnecting entire living cell(s) from the gold electrodes of the BBB. The biological characterization was conducted at −1.50 V for two NIH 3T3 fibroblasts (Figure 5.11A), subconfluent cells with 25% confluence (Figure 5.11B), subconfluent cells with 50% confluence, subconfluent cells with 75% confluence, and confluent cells with 100% confluence (Figure 5.11C). As an evaluation index for the speed of cell detachment at a cellular level, a time required to detach 95% of the adhered cells (CD-time) was measured. The CD-times of the above five cases (averaged from at least 10 measurements) were 45.2 ± 6.8, 36.7 ± 8.7, 31.1 ± 4.2, 24.8 ± 5.5, and 21.1 ± 3.5 s, respectively (Figure 5.11D), showing an inverse proportion to cell confluence. This is because the detachment of a cell applies additional vertical force to neighboring cells through cell−cell interactions at confluent conditions where all cells are connected to each other by the cell−cell interactions. This measurement indicates cell−cell interactions have a correlation to

AU:3

◀ to cell resistive. (C) Contact angles measured from bare gold ($67.3 \pm 2.5°$, left), thiol-treated gold ($53.3 \pm 1.3°$, center), and RTT-functionalized gold ($24.6 \pm 2.8°$, right). (D) XPS survey spectrum of the gold surface modified with RTT. Detected are a gold peak from a gold surface, a sulfur peak from thiol, a nitrogen peak from the amine group of an RGD peptide, and carbon and oxygen peaks from the carboxylic acid group of an RGD peptide. (E) Experimental setup for potentiodynamic electrochemical characterization where the gold surface of the BBB, a platinum electrode, and a Ag/AgCl electrode work as working, counter, and reference electrodes, respectively. (F) CV measured from the gold surface modified with RTT, indicating the reductive desorption of the gold−thiol SAM starts and finishes at −0.90 and −1.65 V, respectively, and gets maximized at −1.50 V.
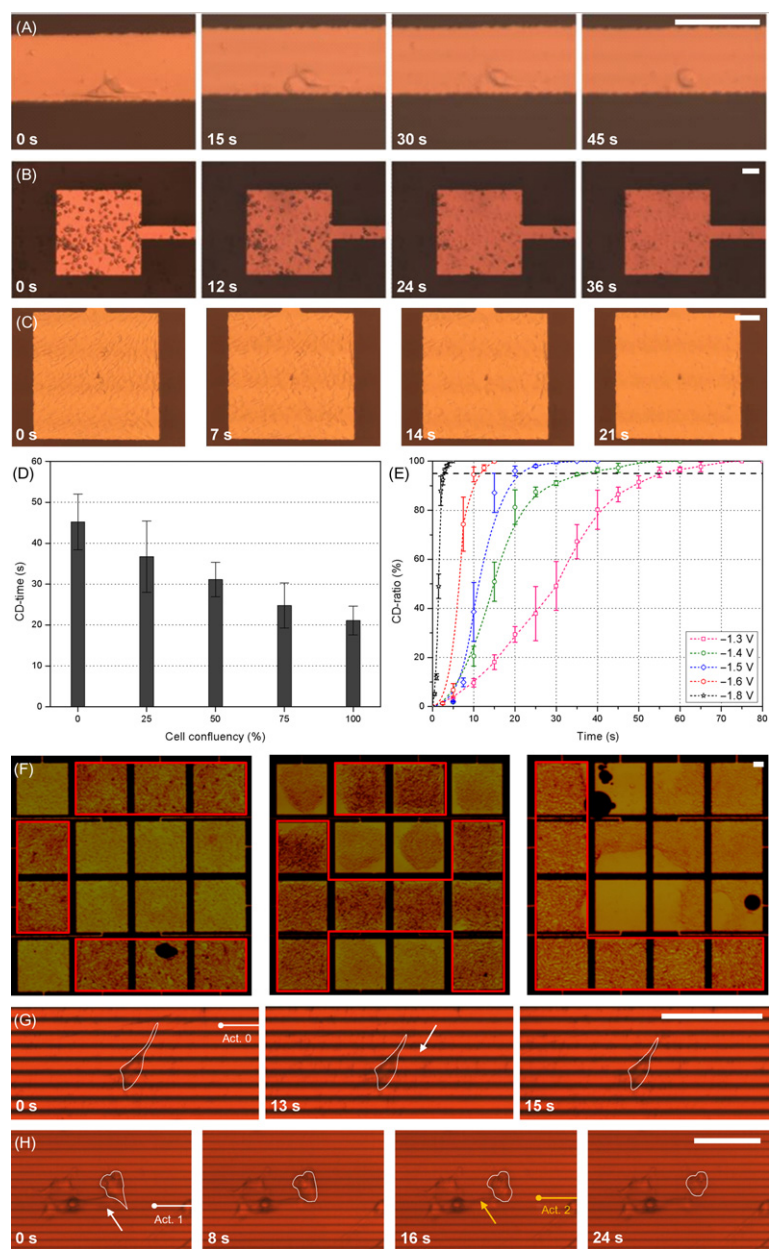
f0060   **FIGURE 5.11**

Spatiotemporal manipulation of cell detachment for the control of cell motility using the BBB. (A−C) ~~Optical sequential~~ images showing the spatiotemporal manipulation of cell

(*Continued*)

cell detachment behavior. The dependence of cell detachment on an activation potential was also investigated by counting the ratio of detached cells to total cells (CD-ratio) as a function of time and activation potential (Figure 5.11E). The CD-ratio increased as the activation potential increased because the reductive desorption of a gold—thiol SAM was in direct proportion to the activation potential (see Figure 5.10F). The measured CD-ratio was monotonically increasing with two inflection points (s-shape curves), demonstrating a large deviation in the strength of integrin binding to extracellular matrix proteins or another cell. A programmable cell patterning was also performed. A single four-by-four BBB was used to spatio-temporally manipulate the detachment of NIH 3T3 fibroblasts at a cellular level (Figure 5.11F). That is, the cells were sequentially patterned in a shape of "C," "A," or "L" using the BBB and then the BBB was reused for the next cell pattern-ing after cleaning it. The BBB was cleaned through two-step cleaning processes (i.e., activation of gold electrodes and simplified organic cleaning of the device). The activation of gold electrodes was for yielding original gold through the reductive desorption of a gold—thiol SAM, and the organic cleaning was for removing bio-logical remnants (e.g., dead cells during cell loading).

p0250   The cell detachment at a subcellular level was also achieved by disconnecting the part of a cell from the BBB having gold lines with a width of 10 μm and a gap of 3 μm (see Figure 5.9C). When we activated a gold line on which one end of the cytoplasm of the cell was placed, the part of the cell was successfully detached and then the detached cytoskeleton finished its retraction within 16 s

◀ detachment at a cellular level for two cells (0% confluent cells), 25% confluent cells, and 100% confluent cells. The two cells are detached from a gold electrode at an activation potential of −1.50 V and their CD-time is 45.2 ± 6.8 s (A). The average CD-time of the 25% confluent cells is 36.7 ± 8.7 s (B). The average CD-time of the 100% confluent cells is 21.1 ± 3.5 s (C). (D) Measured CD-time as a function of cell confluence. This shows the CD-time is in inverse proportion to cell confluence. (E) Measured CD-ratio as a function of time and activation potential for 100% confluent cells. The CD-ratio is monotonically increasing with two inflection points (s-shape curve) indicating there is a large deviation in the strength of integrin binding to extracellular matrix proteins or another cell. (F) Programmable cell patterning using the manipulation of cell detachment on a single four-by-four BBB. The cells are patterned in shapes of "C," "A," and "L," verifying the addressability, multifunctionality, and reusability of the BBB. (G and H) Spatiotemporal manipulation of cell detachment at a subcellular level using the BBB. The part of an NIH 3T3 fibroblast is detached by a single activation (Act. 0). This subcellular detachment is accompanied by the spontaneous retraction of the detached cytoskeleton (G). The part of a cell is sequentially detached by a series of activations (Act. 1 and Act. 2). Scale bars are 100 μm.

AU:7

after subcellular detachment (Figure 5.11G). The retraction speed of the detached cytoskeleton at a subcellular level is faster than that of the detached cell at a cellular level because a single cell which has no constraint in stretching itself is under higher tension than confluent cells. Next, the part of NIH 3T3 fibroblasts was detached with a series of activations (Figure 5.11H). The second activation (Act. 2) was applied 16 s after the first one (Act. 1). This experiment reveals that repetitive activations within dozens of seconds do not sacrifice the viability of the cell and are able to gradually increase the amount of subcellular detachment. These successful manipulations of subcellular detachment open a possibility for the control of cell motility using the BBB. In detail, the movement direction of an adherent cell is controlled by selectively activating some of the gold electrodes of the BBB. When a cell is located on the origin and adheres to four gold electrodes that lie in each quadrant, the cell is thought to move in the first quadrant by activating the gold electrode in the third quadrant (or all gold electrodes except the one in the first quadrant). This is because the RGD peptides tethered on inactivated gold electrode(s) have much higher affinity for cell adhesion than bare gold of activated ones.

5.4 Summary

s0150

p0255 Two MEMS-based, mechanobiological methods for the control of cell motility (i.e., the direction and rate of cell movement) have been presented as preliminary attempts to develop new therapeutic solutions for pathophysiological phenomena related to cell motility. The first method was a Rome platform that passively controls cell movement using diverging micropatterns. The Rome platform was composed of 3 μm thick diverging micropatterns with different divergence angles of $0.5-5.0°$ and two widths of trough/ridge of 3 and 10 μm where divergence begun and ended, respectively. This platform achieved one-directional cell movement (i.e., cell movement in a diverging direction of the diverging micropatterns) by imposing morphological polarity on adherent cells using the diverging micropatterns. The rate of cell movement was controlled by changing two widths of trough/ridge where divergence begun and ended, respectively. The experimental characterizations using the Rome platform inform us of the following biological facts: (i) diverging micropatterns affect the migratory behavior of adherent cells, and the changes in the dimensions and shape of the diverging micropatterns resulted in the changes in the direction and rate of cell movement in a controllable manner; (ii) there are both ceiling and floor values for the dimensions of the diverging micropatterns which can influence cell migration (e.g., the ceiling and floor values for width of trough/ridge are respectively 3 μm (or less) and about $42-49$ μm for NIH 3T3 fibroblasts); (iii) whether the morphological polarization of adherent cells is biological (like *in vivo* cell movement) or artificial (like cell movement on the Rome platform), the morphological polarization is sufficient to

determine the movement direction of the cells; (iv) together with the results of cell movement on multiple, identical micropatterns, cell mechanosensors which receive and respond to external physical cues (e.g., micropatterns in this study) are intensively activated at the circumferential marginal zone of the cell rather than at the central zone. A BBB was also developed as an active method for the control of cell motility. The BBB, composed of multiple gold electrodes patterned on a Pyrex substrate, was surface modified with RTT and PEG to achieve a cell-adhesive surface on the gold electrodes and a cell-resistive surface on the Pyrex substrate, respectively. This assay controlled cell detachment at a subcellular level by reductively desorbing a gold−thiol SAM with an activation potential of −0.90 to −1.65 V. When the chemical binding between gold and thiol was broken by activating a gold electrode of interest, one part of a cell, located on the electrode, was detached from the activated gold electrode and then experienced its fast retraction. The detached (and then retracting) cytoskeleton experienced a 3 times decrease in its elastic modulus and also a 30 times increase in its damping coefficient within a few seconds. In the manipulation of cell movement using the BBB, one part of a cell which was relatively in the opposite direction of intended cell movement was deliberately detached. The detached cytoskeleton was spontaneously retracted, which lead to the successful control of cell movement.

p0260   The extrapolation of these MEMS-based, mechanobiological methods to other cells might help us to better understand the migratory nature of adherent cells, thereby resulting in a development of new therapeutic strategies related to cell movement. Ongoing work is focusing on more in-depth control of cell motility by developing large-scale assays to shed light on the dynamics of cell motility. Combined with molecular dynamics models [52−54], the proposed devices for the programmable control of cell movement will offer an opportunity for studies of molecular cell biomechanics related to cell motility.

References

[1] D.A. Lauffenburger, A.F. Horwitz, Cell migration: a physically integrated molecular process, Cell 84 (1996) 359−369.

[2] A.J. Ridley, M.A. Schwartz, K. Burridge, R.A. Firtel, M.H. Ginsberg, G. Borisy, et al., Cell migration: integrating signals from front to back, Science 302 (2003) 1704−1709.

[3] V. Jones, K. Harding, J. Stechmiller, G. Schultz, Acute and chronic wound healing, in: S. Baranoskiand, E.A. Ayello (Eds.), Wound Care Essentials: Practice Principles, Lippincott Williams & Wilkins, 2008, pp. 64−76.   AU:4

[4] G.C. Gurtner, S. Werner, Y. Barrandon, M.T. Longaker, Wound repair and regeneration, Nature 453 (2008) 314−321.

[5] J.Y. Lim, H.J. Donahue, Cell sensing and response to micro- and nanostructured surfaces produced by chemical and topographic patterning, Tissue Eng. 13 (2007) 1879−1891.

[6] M.N. Yousaf, B.T. Houseman, M. Mrksich, Using electroactive substrates to pattern the attachment of two different cell types, Proc. Natl. Acad. Sci. U.S.A. 98 (2001) 5992−5996.

[7] A. Tourovskaia, T. Barber, B.T. Wickes, D. Hirdes, B. Grin, D.G. Castner, et al., Micropatterns of chemisorbed cell adhesion−repellent films using oxygen plasma etching and elastomeric masks, Langmuir 19 (2003) 4754−4764.

[8] S.P. Massia, J.A. Hubbell, An RGD spacing of 440 nm is sufficient for integrin $\alpha_v\beta_3$-mediated fibroblast spreading and 140 nm for focal contact and stress fiber formation, J. Cell Biol. 114 (1991) 1089−1100.

[9] K.Y. Lee, E. Alsberg, S. Hsiong, W. Comisar, J. Linderman, R. Ziff, et al., Nanoscale adhesion ligand organization regulates osteoblast proliferation and differentiation, Nano. Lett. 4 (2004) 1501−1506.

[10] A.M. Green, J.A. Jansen, J.P. van der Waerden, A.F. von Recum, Fibroblast response to microtextured silicone surfaces: texture orientation into or out of the surface, J. Biomed. Mater. Res. 28 (1994) 647−653.

[11] M.J. Dalby, D. Giannaras, M.O. Riehle, N. Gadegaard, S. Affrossman, A.S. Curtis, Rapid fibroblast adhesion to 27 nm high polymer demixed nano-topography, Biomaterials 25 (2004) 77−83.

[12] X.F. Walboomers, W. Monaghan, A.S. Curtis, J.A. Jansen, Attachment of fibroblasts on smooth and microgrooved polystyrene, J. Biomed. Mater. Res. 46 (1999) 212−220.

[13] F. Johansson, P. Carlberg, N. Danielsen, L. Montelius, M. Kanje, Axonal outgrowth on nano-imprinted patterns, Biomaterials 27 (2006) 1251−1258.

[14] C.D. Nobes, A. Hall, Rho GTPases control polarity, protrusion, and adhesion during cell movement, J. Cell Biol. 144 (1999) 1235−1244.

[15] S. Etienne-Manneville, A. Hall, Integrin-mediated activation of Cdc42 controls cell polarity in migrating astrocytes through PKCzeta, Cell 106 (2001) 489−498.

[16] A. Kodama, I. Karakesisoglou, E. Wong, A. Vaezi, E. Fuchs, ACF7: an essential integrator of microtubule dynamics, Cell 115 (2003) 343−354.

[17] R.G. Harrison, The reaction of embryonic cells to solid structures, J. Exp. Zool. A Ecol. Genet. Physiol. 17 (1914) 521−544.

[18] C. Oakley, D.M. Brunette, Response of single, pairs, and clusters of epithelial cells to substratum topography, Biochem. Cell Biol. 73 (1995) 473−489.

[19] A. Curtis, C. Wilkinson, Topographical control of cells, Biomaterials 18 (1997) 1573−1583.

[20] X.F. Walboomers, H.J. Croes, L.A. Ginsel, J.A. Jansen, Growth behaviour of fibroblasts on microgrooved polystyrene, Biomaterials 19 (1998) 1861−1868.

[21] D.M. Brunette, B. Chehroudi, The effects of the surface topography of micromachined titanium substrata on cell behavior *in vitro* and *in vivo*, J. Biomech. Eng. 121 (1999) 49−57.

[22] Y.A. Rovensky, V.I. Samoilov, Morphogenetic response of cultured normal and transformed fibroblasts, and epitheliocytes, to a cylindrical substratum surface. Possible role for the actin filament bundle pattern, J. Cell Sci. 107 (1994) 1255−1263.

[23] K. Kolind, A. Dolatshahi-Pirouz, J. Lovmand, F.S. Pedersen, M. Foss, F. Besenbacher, A combinatorial screening of human fibroblast responses on microstructured surfaces, Biomaterials 31 (2010) 9182−9191.

[24] H. Jeon, H. Hidai, D.J. Hwang, K.E. Healy, C.P. Grigoropoulos, The effect of micronscale anisotropic cross patterns on fibroblast migration, Biomaterials 31 (2010) 4286−4295.

[25] S. Takeuchi, Wound healing in the cornea of the chick embryo. III. The influence of pore size of millipore filters on the migration of isolated epithelial sheets in culture, Dev. Biol. 51 (1976) 49−62.

[26] H.J. Fitton, B.A. Dalton, G. Beumer, G. Johnson, H.J. Griesser, J.G. Steele, Surface topography can interfere with epithelial tissue migration, J. Biomed. Mater. Res. A 42 (1998) 245−257.

[27] N.L. Jeon, H. Baskaran, S.K.W. Dertinger, G.M. Whitesides, L. Van de Water, M. Toner, Neutrophil chemotaxis in linear and complex gradients of interleukin-8 formed in a microfabricated device, Nat. Biotechnol. 20 (2002) 826−830.

[28] F. Lin, C. Nguyan, S. Wang, W. Saadi, S. Gross, N.L. Jeon, Neutrophil migration in opposing chemoattractant gradients using microfluidic chemotaxis devices, Ann. Biomed. Eng. 33 (2005) 475−482.

[29] J.P. Diao, L. Young, S. Kim, E.A. Fogarty, S.M. Heilman, P. Zhou, et al., A three-channel microfluidic device for generating static linear gradients and its application to the quantitative analysis of bacterial chemotaxis, Lab Chip 6 (2006) 381−388.

[30] C.W. Frevert, G. Boggy, T.M. Keenan, A. Folch, Measurement of cell migration in response to an evolving radial chemokine gradient triggered by a microvalve, Lab Chip 6 (2006) 849−856.

[31] S. Koyama, D. Amarie, H. Soini, M. Novotny, S.C. Jacobson, Chemotaxis of mouse sperm on microfluidic devices, Anal. Chem. 78 (2006) 3354−3359.

[32] N. Blow, Cell migration: our protruding knowledge, Nat. Methods 4 (2007) 589−594.

[33] P. Clark, P. Connolly, A.S. Curtis, J.A. Dow, C.D. Wilkinson, Topographical control of cell behavior. I. Simple step cues, Development 99 (1987) 439−448.

[34] B. Chehroudi, T.R. Gould, D.M. Brunette, Titanium-coated micromachined grooves of different dimensions affect epithelial and connective-tissue cells differently *in vivo*, J. Biomed. Mater. Res. 24 (1990) 1203−1219.

[35] J.W. Lussi, C. Tang, P.-A. Kuenzi, U. Staufer, G. Csucs, J. Vörös, et al., Selective molecular assembly patterning at the nanoscale: a novel platform for producing protein patterns by electron-beam lithography on SiO_2/indium tin oxide-coated glass substrates, Nanotechnology 16 (2005) 1781−1786.

[36] K.-B. Lee, S.J. Park, C.A. Mirkin, J.C. Smith, M. Mrksich, Protein nanoarrays generated by dip-pen nanolithography, Science 295 (2002) 1702−1705.

[37] J.D. Hoff, L.-J. Cheng, E. Meyhöfer, L.J. Guo, A.J. Hunt, Nanoscale protein patterning by imprint lithography, Nano. Lett. 4 (2004) 853−857.

[38] C.S. Chen, M. Mrksich, S. Huang, G.M. Whitesides, D.E. Ingber, Geometric control of cell life and death, Science 276 (1997) 1425−1428.

[39] N.Y. Lee, J.R. Lim, Y.S. Kim, Selective patterning and immobilization of biomolecules within precisely-defined micro-reservoirs, Biosens. Bioelectron. 21 (2006) 2188−2193.

[40] A. Folch, B.H. Jo, O. Hurtado, D.J. Beebe, M. Toner, Microfabricated elastomeric stencils for micropatterning cell cultures, J. Biomed. Mater. Res. 52 (2000) 346−353.

[41] E.A. Roth, T. Xu, M. Das, C. Gregory, J.J. Hickman, T. Boland, Inkjet printing for high-throughput cell patterning, Biomaterials 25 (2004) 3707−3715.

[42] A.L. Birkbeck, R.A. Flynn, M. Ozkan, D. Song, M. Gross, S.C. Esener, VCSEL arrays as micromanipulators in chip-based biosystems, Biomed. Microdevices 5 (2003) 47−54.

[43] B. Alberts, A. Johnson, J. Lewis, M. Raff, K. Roberts, P. Walter, Molecular Biology of the Cell, Garland Science, 2002.   AU:5

[44] S.-H. Yoon, Y.-H. Cho, High-precision digital microflow controllers using fluidic digital-to-analog converters composed of binary-weighted flow resistors, J. Microelectromech. Syst. 15 (2006) 967−975.

[45] D.I. Shreiber, V.H. Barocas, R.T. Tranquillo, Temporal variations in cell migration and traction during fibroblast-mediated gel compaction, Biophys. J. 84 (2003) 4102−4114.

[46] R.B. Dickinson, R.T. Tranquillo, Optimal estimation of cell movement indexes from the statistical analysis of cell tracking data, AIChE J. 39 (1993) 1995−2010.

[47] P.A. DiMilla, J.A. Stone, J.A. Quinn, S.M. Albelda, D.A. Lauffenburger, Maximal migration of human smooth muscle cells on fibronectin and type IV collagen occurs at an intermediate attachment strength, J. Cell Biol. 122 (1993) 729−737.

[48] J. Tan, W.M. Saltzman, Topographical control of human neutrophil motility on micropatterned materials with various surface chemistry, Biomaterials 23 (2002) 3215−3225.

[49] C.L. Stokes, D.A. Lauffenburger, S.K. Williams, Migration of individual microvessel endothelial cells: stochastic model and parameter measurement, J. Cell Sci. 99 (1991) 419−430.

[50] G. Karp, Cell and Molecular Biology: Concepts and Experiments, John Wiley & Sons, 2005.   AU:6

[51] B.A. Dalton, X.F. Walboomers, M. Dziegielewski, M.D. Evans, S. Taylor, J.A. Jansen, et al., Modulation of epithelial tissue and cell migration by microgrooves, J. Biomed. Mater. Res. 56 (2001) 195−207.

[52] S.E. Lee, S. Chunsrivirot, R.D. Kamm, M.R.K. Mofrad, Molecular dynamics study of talin−vinculin binding, Biophys. J. 95 (2008) 2027−2036.

[53] J. Golji, M.R.K. Mofrad, A molecular dynamics investigation of vinculin activation, Biophys. J. 99 (2010) 1073−1081.

[54] J. Golji, J. Lam, M.R.K. Mofrad, Vinculin activation is necessary for complete talin binding, Biophys. J. 100 (2011) 332−340.

NON-PRINT ITEM

Abstract

Directed cell motility is critical for a wide range of biological and physiological processes. Although several nano/microtopographical patterns (e.g., parallel grooves, cross patterns, and three-dimensional post arrays) have been used to guide cell motility, a full control for the direction and rate of cell movement has still remained challenging. This motives us to develop microelectromechanical systems (MEMS)-based, mechanobiological approaches which control the motility of adherent cells. This chapter presents two methods, each of which respectively controls cell motility (i.e., movement) in passive and active ways. The passive control of cell motility is achieved by introducing diverging micropatterns, termed "Rome platforms," to adherent cells. The diverging micropatterns provide adherent cells with directionality for cell motility by imposing one-directional morphological polarization on the cells, thus forcing the cells to move in the diverging direction of the diverging micropatterns; the rate of cell movement is controlled not by adjusting the divergence angle of the micropatterns but by changing two widths of trough/ridge at which divergence begins and ends, respectively. The active control of cell motility is made by selectively detaching one part of an adherent cell from a substrate using biological breadboards (BBBs). The BBBs are composed of multiple gold electrodes patterned on a Pyrex glass. The gold electrodes and Pyrex glass of the BBBs are surface modified with arginine−glycine−aspartic acid-terminated thiol and polyethylene glycol, respectively. The BBBs spatiotemporally manipulate cell detachment using the reductive desorption of a gold−thiol self-assembled monolayer at an activation potential of −0.90 to −1.65 V, thus controlling the motility of adherent cells. These two approaches using MEMS technology show a potential for thoroughly controlling biological and physiological phenomena related to cell motility and are expected to lead to better understanding of biomechanics, especially cell dynamics.

Key Words

Biological breadboard, cell motility, diverging micropattern, MEMS, Rome platform